Mott insulating state of IrO₆ honeycomb monolayer structured in ilmenite-type oxide superlattice

Masamichi Negishi [1,2,*] Kohei Fujiwara [1,3] Seong-Hoon Jang [1,4] Yi-Feng Zhao [4,5] Shun Sasano [6] Ryo Ishikawa [6]
Naoya Shibata [6,7] Daisuke Shiga [8] Hiroshi Kumigashira [8] Yuto Nakamura [9] Hideo Kishida [9]
Yukitoshi Motome [4] and Atsushi Tsukazaki [1,4,10,11,†]

[1]*Institute for Materials Research, Tohoku University, Sendai 980–8577, Japan*
[2]*Department of Chemistry, Tohoku University, Sendai 980–8578, Japan*
[3]*Department of Chemistry, Rikkyo University, Tokyo 171–8501, Japan*
[4]*Department of Applied Physics, The University of Tokyo, Tokyo 113–8656, Japan*
[5]*Department of Physics, Arizona State University, Tempe, Arizona 85287, USA*
[6]*Institute of Engineering Innovation, The University of Tokyo, Tokyo 113–8656, Japan*
[7]*Nanostructures Research Laboratory, Japan Fine Ceramics Center, Nagoya 456–8587, Japan*
[8]*Institute of Multidisciplinary Research for Advanced Materials (IMRAM), Tohoku University, Sendai 980–8577, Japan*
[9]*Department of Applied Physics, Nagoya University, Nagoya 464–8603, Japan*
[10]*Center for Science and Innovation in Spintronics (CSIS), Tohoku University, Sendai 980–8577, Japan*
[11]*Quantum-Phase Electronics Center (QPEC), The University of Tokyo, Tokyo 113–8656, Japan*

Quantum magnetism based on the Kitaev honeycomb model has been intensively studied both by theoretical material design and experimental materialization. In contrast to the considerable progress of theoretical modeling and experiments on bulk crystals, it is still difficult to find a candidate material applicable to thin films and devices toward future quantum computation. Here we clearly demonstrate a Mott insulating state of IrO₆ honeycomb monolayer structured in ilmenite-type Mg-Ir-O/MgTiO₃ superlattices, which is a good candidate of the Kitaev honeycomb magnet applicable to devices. Electronic states detected by photoelectron spectroscopy agree well with those in theoretical band calculations. The stabilized superlattice with the Mott gap state is a promising platform to examine the device physics of the Majorana fermions and the Z_2 fluxes in the Kitaev honeycomb model, suggesting the thin-film techniques are quite beneficial for triggering the exploration of quantum computation in designable and evolvable heterostructures.

I. INTRODUCTION

Materialization of a quantum magnet called the Kitaev honeycomb magnet, which is based on the theoretical proposals of Kitaev's honeycomb spin model [1,2], has been rapidly progressed both in theory and in experiment [3,4]. An interesting feature of the Kitaev honeycomb magnet is its unique ground state of quantum spin liquid; the realization of a quantum spin liquid has long been one of the unsolved problems in research of quantum magnetism [5]. In low-energy excitations in the Kitaev honeycomb magnet, the spins are expected to be fractionalized into itinerant Majorana fermions and Z_2 fluxes [1,3,4]. These unique quantum states make the Kitaev honeycomb magnet a good playground to implement topological quantum computing [1].

Previous studies on the Kitaev honeycomb magnet have been performed mainly using bulk samples, because some physical properties which can be measured in bulk samples reflect the unique features of the magnetism [4]. Representative candidates of the Kitaev honeycomb magnet are α-RuCl₃ and iridium oxides with layered honeycomb structures variated from α-Li₂IrO₃ and Na₂IrO₃ [2,3]. Conventional ways to detect the nonexistence of long-range magnetic orders in these candidates are measuring magnetic susceptibility [6–8], heat capacity [7,9,10], neutron scattering [11], and Raman shift [12,13]. In addition, thermal Hall measurement is considered as a powerful technique to evidence formation of the Kitaev honeycomb magnet. In the thermal Hall effect of a single crystal of α-RuCl₃, a half-integer quantized state was observed [14]. Although it may link to a magnon-related mechanism [15,16], this half-integer quantized thermal Hall effect is considered to be convincing evidence of the formation of itinerant Majorana fermions [14]. Further approaches to detect the Majorana fermions have been theoretically proposed via spin transport measurements [17–20] and direct observation of the quasiparticles by scanning tunneling microscopy [21–25]. To conduct such advanced experiments, it is necessary to develop ways to synthesize thin films and devices of the Kitaev honeycomb magnet. For α-RuCl₃, exfoliation of single crystals
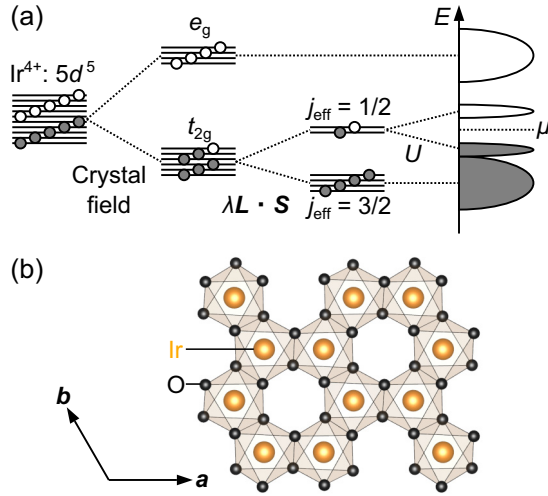
FIG. 1. (a) A schematic band diagram of Ir^{4+}-content oxides for materializing the $J_{eff} = 1/2$ Mott insulating electronic state. (b) A honeycomb layer of IrO_6 octahedra in ilmenite $MgIrO_3$.

to make $RuCl_3$ nanosheets [26–28] and heterostructures of $RuCl_3$ nanosheets and graphene [29–31] have been studied. Another method to synthesize thin films and heterostructures is direct deposition of thin films in high-vacuum chambers, which could realize much cleaner interfaces between materials compared with the exfoliation method. However, there are only a few material platforms of the Kitaev honeycomb magnet applicable to direct deposition of thin films and heterostructures because of the difficulty described below; the representative candidates of the Kitaev honeycomb magnet with Ir and Ru honeycomb structure contain volatile elements, halide Cl or alkaline metal Li or Na, which make it difficult to grow thin films of the materials in clean high-vacuum environments.

Here we aim to synthesize oxide thin films of a candidate of the Kitaev honeycomb magnet for detection of the $J_{eff} = 1/2$ Mott insulating state [illustrated in Fig. 1(a)] leading to the itinerant Majorana fermions and localized Z_2 fluxes. Oxide-thin-film techniques enable us to stabilize honeycomb monolayers in epitaxial superlattice [32,33] and, by forming heterostructures with various oxides, to modify the Kitaev honeycomb magnetism via interface interactions and/or lattice distortions [34,35]. To form thin films of the Kitaev honeycomb magnet, we focused on ilmenite-type iridate $MgIrO_3$. Ilmenite-type $MgIrO_3$ contains Ir^{4+} ions and honeycomb layers of edge-shared IrO_6 octahedra as shown in Fig. 1(b). This IrO_6 honeycomb structure meets one of the necessary conditions to realize the Kitaev honeycomb magnet in iridates [2]. As shown in Fig. 1(a), the $5d$ electronic states of Ir^{4+} in an IrO_6 octahedron split to e_g and t_{2g} orbitals by crystal field. The t_{2g} orbitals split to $j_{eff} = 3/2$ and $1/2$ states by spin-orbit interaction. Filling five electrons into these states results in the half-filled $j_{eff} = 1/2$ states, which form a multielectron state with effective total angular momentum $J_{eff} = 1/2$. Finally, the Coulomb interaction forms a Mott gap in the $J_{eff} = 1/2$ state [36]. Typical values of octahedral crystal field splitting, spin-orbit coupling λ, and Coulomb repulsion U in iridates are about 2 eV, 0.4 eV, and 3 eV, respectively [37,38]. In the

previous study, only powder samples of ilmenite-type $MgIrO_3$ were obtained by a topotactic reaction from layered honeycomb $\alpha\text{-}Li_2IrO_3$ [39]. To the best of our knowledge, there is no report of single crystals and thin films of ilmenite-type $MgIrO_3$. We have reported difficulty in crystalline formation of thick films of single-phase ilmenite-type $MgIrO_3$ on $Al_2O_3(0001)$ substrates by pulsed-laser deposition [40] due to the metastability of $MgIrO_3$, which resulted in phase separation to stable MgO and Ir or IrO_2. Here we attempted stabilization of IrO_6 honeycomb layers by a superlattice technique according to the previous research on successful synthesis of IrO_6 honeycomb monolayers in Mn-Ir-O/$MnTiO_3$ superlattices [33]. In this study, we fabricated Mg-Ir-O/$MgTiO_3$ superlattices to stabilize IrO_6 honeycombs by pulsed-laser deposition on Al_2O_3 substrates. Structural characterization and experimental detection of the electronic states were conducted to detect the Mott gap states by theoretical supports with band calculations.

II. METHODS

Two $MgTiO_3$-capped [$MgTiO_3$, Mg-Ir-O]$_3$ superlattices, a Mg-Ir-O/$MgTiO_3$ heterostructure, and a $MgTiO_3$ single-layer film were deposited on $\alpha\text{-}Al_2O_3(0001)$ substrates by pulsed-laser deposition with a KrF excimer laser (wavelength = 248 nm). All the Mg-Ir-O layers were deposited by alternate ablation of MgO and $MgO\text{-}2IrO_2$ targets, while the $MgTiO_3$ layers were deposited from a $MgTiO_3$ target. Details of preparation and evaluation of the $MgO\text{-}2IrO_2$ and $MgTiO_3$ targets are described in Refs. [40,41], respectively. Oxygen pressure inside the growth chamber was kept at 1×10^{-3} Pa during depositions. Laser fluence on the targets was set at $0.85 \, J/cm^2$ for $MgTiO_3$ and at $1.93 \, J/cm^2$ for MgO and $MgO\text{-}2IrO_2$, respectively. In deposition of the superlattices, the first 5–7-nm-thick $MgTiO_3$ layer was deposited at $800\,°C - 820\,°C$, and then the following Mg-Ir-O and $MgTiO_3$ layers were deposited at $500\,°C$, terminated by $MgTiO_3$ as a capping layer. After deposition, the superlattice samples were annealed at $600\,°C–700\,°C$ in air for 24 h to improve crystallinity of the $MgTiO_3$ layers. The $MgTiO_3$ film was prepared in an analogous way to the superlattices; deposition of the first 8 nm of the $MgTiO_3$ layer at $800\,°C - 820\,°C$, followed by deposition of the rest of the 18 nm of the $MgTiO_3$ layer at $500\,°C$, and finally, the *ex situ* annealing. On the other hand, in preparation of the Mg-Ir-O/$MgTiO_3$ heterostructure, whose stacking structure was optimized for x-ray photoelectron spectroscopy (XPS), the 20-nm-thick $MgTiO_3$ layer was deposited at $500\,°C$ and annealed above $800\,°C$ inside the growth chamber for 2 h to balance surface flatness and crystallinity of the relatively thick $MgTiO_3$ layer. After that, the 1-nm-thick Mg-Ir-O layer was deposited at $500\,°C$. XPS measurements were performed after *ex situ* transfer. Considering the possibility of evaporation of iridium oxides at high temperature, no *ex situ* annealing was performed on the Mg-Ir-O/$MgTiO_3$ heterostructure.

The *ab initio* calculations, including structure optimizations for the bulk and the monolayer cases of $MgIrO_3$, were performed by using quantum espresso [42]. We adopted LDA + SOC + U by including the Hubbard correction to the Ir $5d$ orbitals with the Coulomb repulsion: $U = 3$ eV [43].
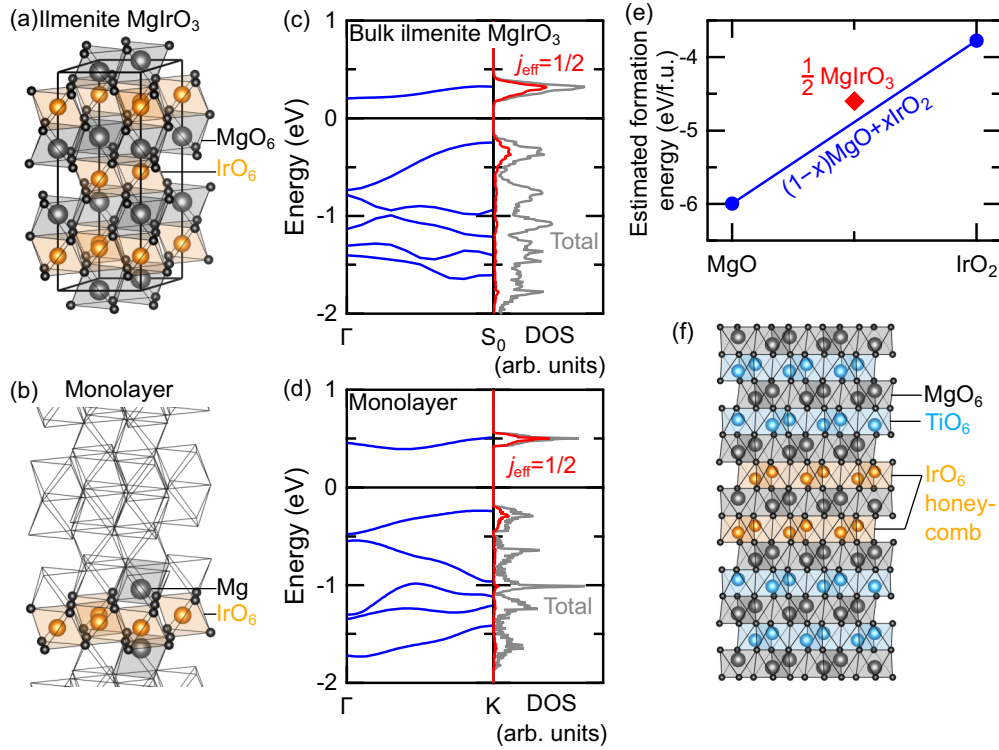
FIG. 2. Calculation of electronic states of ilmenite MgIrO$_3$ and IrO$_6$ monolayer. (a) and (b) Crystal structure of ilmenite MgIrO$_3$ (a) and IrO$_6$ monolayer (b). (c) and (d) Calculated band structures of ilmenite MgIrO$_3$ (c) [47] and monolayer (d). (e) Estimated formation energy of ilmenite MgIrO$_3$ displayed with those of rocksalt MgO and rutile IrO$_2$ [57,58]. (f) An ideal crystal structure of Mg-Ir-O/MgTiO$_3$ superlattice.

Then, we constructed maximally localized Wannier functions of Ir $5d$ t_{2g} and O $2p$ orbitals [44–46]. From the results, we computed the density of states (DOS) projected onto the spin-orbit-coupled (SOC) bases labeled by the effective angular momentum j_{eff} and O $2p$ orbitals. The details for the bulk and the monolayer cases are given in Refs. [47,35], respectively. The value of Coulomb repulsion was selected based on Ref. [38]. These theoretical calculations were independently carried out with experimental results. Meanwhile, the formation energy of the bulk MgIrO$_3$ was calculated by using Vienna *ab initio* Simulation Package [48–52] and the Computational Phase Diagram App provided by the Materials Project given the competing phase of Mg-Ir-O [53,54].

The electron-transparent thin specimen was prepared by mechanical polishing and Ar ion beam milling performed at 0.5 kV in the final stage. By applying an aberration-corrected scanning transmission electron microscopy (STEM, ARM300CF) equipped with a Delta-type corrector and a cold field-emission gun operated at 300 kV, atomic arrangements and crystalline uniformity are characterized to examine the ilmenite superlattice structure. The convergence and collection semiangles were 30 mrad and 90–200 mrad, respectively. To improve the signal-to-noise ratio, the sequential averaging method was used for annular dark-field (ADF)-STEM images [55]. X-ray reflectivity (XRR) and x-ray diffraction (XRD) measurements were performed using an x-ray diffractometer with the Cu $K\alpha_1$ radiation. XPS was performed using a home-built spectrometer with R3000 electron energy analyzer and a monochromatized Al $K\alpha$ x-ray source (Scienta Omicron Co., Ltd.). The XPS measurements were carried out at room temperature, whose energy resolution was about 0.50 eV for the pass energy of 100 eV and about 0.79 eV for the pass energy of 200 eV. All XPS data except for the survey scan shown in the Supplemental Material [56] were measured with the pass energy of 100 eV. The beam was monochromatized and unpolarized. All spectra were taken at normal emission geometry. Two Au(100 nm)/Ti(5 nm) electrodes separated by a 2-mm-wide window were deposited on the surface of the sample to prevent the surface charging of the sample during the XPS measurements. These gold electrodes caused negligibly weak signals in the measurements with the pass energy of 100 eV, as shown in the Supplemental Material [56]. All spectra were calibrated relative to the C $1s$ signal located at 284.42 eV. Measurements of optical absorption were performed using a multiple reflection technique by oblique incidence with fiber optics as shown in Fig. S2(a) [56]. The edges of the Al$_2$O$_3$ substrates were polished to 45 degrees. In the optical measurements above 1.2 eV, a light source MINI-D2T (Ocean Optics) and a detector HR2000CG-UV-NIR (Ocean Optics) were used. Below 1.2 eV, a light source LS-1 tungsten halogen lamp (Ocean Optics) and a detector AvaSpec-NIR256-1.7 (Avantes) were used.

A list of the samples and the measurements performed on them is shown as Table SI [56].

III. RESULTS

Theoretical calculations on bulk ilmenite-type MgIrO$_3$ [Fig. 2(a)] and IrO$_6$ honeycomb monolayer in MgIrO$_3$ [Fig. 2(b)] were conducted to examine the electronic band
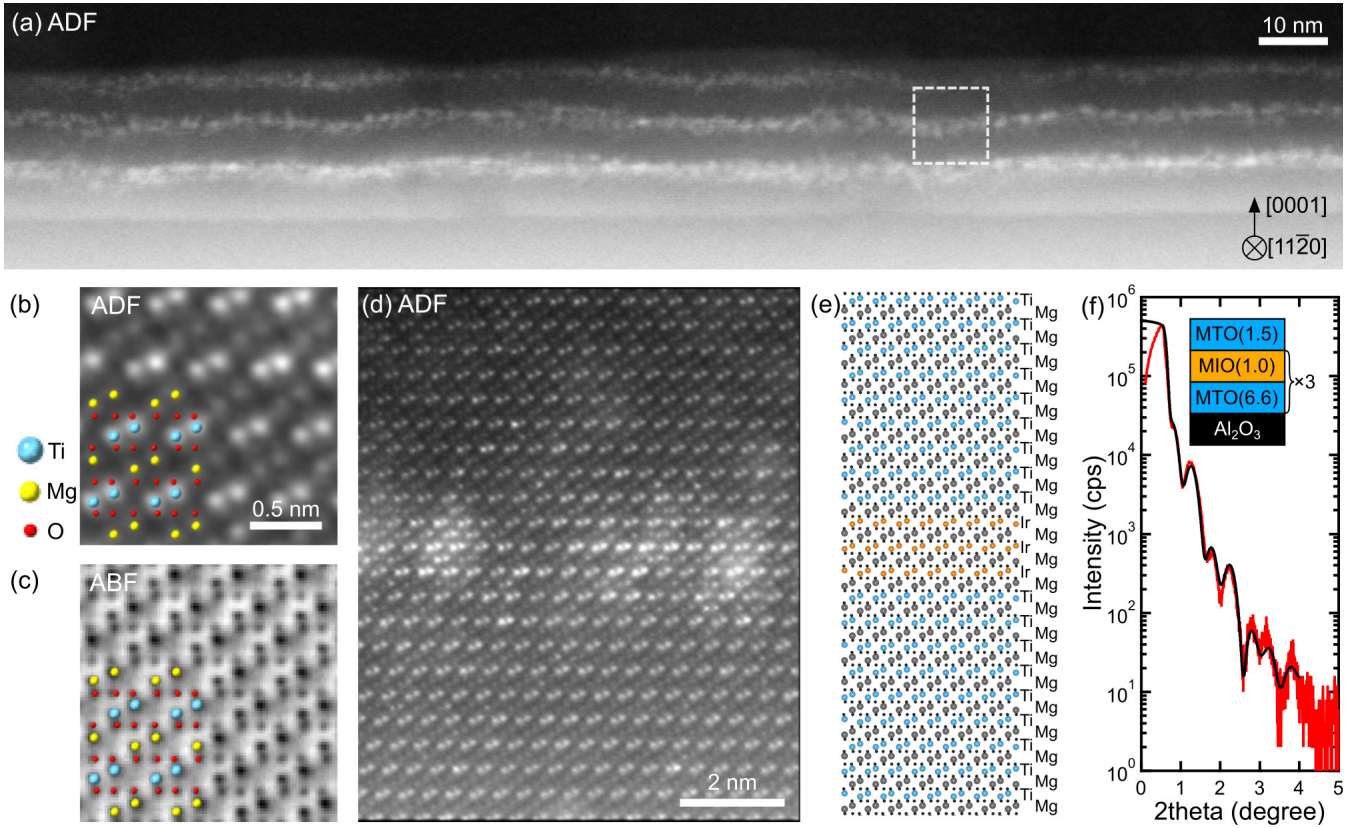
FIG. 3. Structural characterization of the superlattice. (a) A large field-of-view ADF-STEM image. (b) and (c) ADF- and ABF-STEM images focused on an area of $MgTiO_3$, respectively. (d) An ADF-STEM image focused on the area around the dashed box in (a). (e) An ideal crystal structure of $MgTiO_3$/Mg-Ir-O/$MgTiO_3$ heterostructure corresponding to (d). (f) XRR result of the identical sample. The black curve: the fitting result corresponding to the stacking structure shown in the inset. In the inset, thickness values in units of nanometers of $MgTiO_3$ (MTO) and Mg-Ir-O (MIO) layers are shown as parentheses.

structures and projected DOS. Comparing bulk $MgIrO_3$ and monolayer in Figs. 2(c) and 2(d), both band structures clearly demonstrate formation of the $J_{eff} = 1/2$ Mott insulating state with gap formation at the Fermi level. The projected DOS-s show that both highest occupied and lowest empty bands are mainly composed of the Ir $j_{eff} = 1/2$ states. In Fig. 2(d) the four states located from -2 to -0.6 eV just below the $j_{eff} = 1/2$ states correspond to the Ir $j_{eff} = 3/2$ states, while the states below -2.5 eV correspond to the O $2p$ states. The DOS-s projected on the Ir $j_{eff} = 3/2$ and the O $2p$ states are shown in Fig. S1 [56]. These features of the band structures in the monolayer indicate that electronic states of ilmenite-type $MgIrO_3$ remain with the Ir $J_{eff} = 1/2$ Mott insulating state [36]. Because the IrO_6 honeycomb structure and the Ir $J_{eff} = 1/2$ Mott insulating state are both necessary conditions of the Kitaev honeycomb magnet in iridates, these two materials are expectedly good candidates of the Kitaev honeycomb magnet.

To evaluate stability of ilmenite-type $MgIrO_3$, we calculated the formation energy of ilmenite $MgIrO_3$ and compared it with those of rocksalt MgO (mp-1265) and rutile IrO_2 (mp-2723) reported in the Materials Project [57,58] [Fig. 2(e)]. The formation energy of ilmenite $MgIrO_3$ we calculated is -9.208 eV/f.u., which is higher than the sum of those of MgO and IrO_2, -9.772 eV/f.u., indicating that ilmenite $MgIrO_3$ is a metastable phase. Our previous study on Mg-Ir-O films deposited on Al_2O_3(0001) substrates [40], in

which the films were composed of MgO and IrO_2 (or Ir) instead of ilmenite $MgIrO_3$, is consistent with these calculations of formation energy in terms of thermodynamic stability. Considering this difficulty to stabilize the ilmenite structure of $MgIrO_3$, we aimed to form IrO_6 honeycomb layers in 1-nm-thick Mg-Ir-O layers in ilmenite-based superlattice [33] [$MgTiO_3$, Mg-Ir-O], as displayed in Fig. 2(f). Since $MgTiO_3$ is a nonmagnetic d^0 insulator [41], the electronic band structure near the Fermi level and a magnetic state of Mg-Ir-O are not affected by the $MgTiO_3$ in the superlattice structures.

For structural characterization, one of the superlattices of $MgTiO_3$/[$MgTiO_3$, Mg-Ir-O]$_3$/Al_2O_3(0001) was measured by atomic-resolution STEM. Figure 3(a) displays an ADF image of a roughly 180-nm-wide area. In the ADF image of Fig. 3(a), three bright layers were observed; these three layers correspond to the three Mg-Ir-O layers in the superlattice structure, because atomic column containing the heavier Ir are visualized as brighter contrasts owing to the Z-contrast nature (Z is the atomic number) [59]. To clarify the ilmenite structure, the magnified ADF and annular bright-field (ABF) STEM images at the area of $MgTiO_3$ are compared in Figs. 3(b) and 3(c), respectively. Alignment of bright dimers and dark dimers in the ADF image of Fig. 3(b) are well consistent with the structural model of ilmenite-type $MgTiO_3$ with Ti and Mg ions, respectively. In the ABF image of Fig. 3(c), positions of O atomic columns are clearly visible

in addition to those of Ti and Mg atomic columns. These positions of O ions also agree with the ilmenite structure. Based on the ilmenite structure of MgTiO$_3$, IrO$_6$ honeycomb layers were expectedly stabilized well in the superlattice. Figure 3(d) is an ADF image focused on the area displayed in Fig. 3(a) by the white dashed outline. The corresponding ABF image is shown in the Supplemental Material [56]. The bright area at the center of the image indicates the Mg-Ir-O layer containing Ir, which is sandwiched by the top and bottom ilmenite-type MgTiO$_3$ layers. Compared with the structural model of an ideal MgTiO$_3$/Mg-Ir-O/MgTiO$_3$ heterostructure shown in Fig. 3(e), Ir ions are mainly located at the Ti sites of the ilmenite-type structure, although some Ir ions are located at the Mg sites. Such intersite mixing between Ir and Mg may appear as an inhomogeneous small region due to the energetically stable ilmenite derivatives, corresponding to the formation of random-corundum or LiNbO$_3$ structure. Therefore, we observe that the IrO$_6$ honeycomb monolayer was stabilized in ilmenite-type oxide superlattice with the partial random distribution of Ir ions. In addition to the STEM observations, we also performed XRR measurement to evaluate superlattice stacking structure of our sample. Figure 3(f) shows the XRR result measured on the identical sample shown in Figs. 3(a)–3(d). The spectrum shows oscillation reflecting the superlattice structure. The oscillation agrees well with the black curve obtained by curve fitting, which corresponds to the structural model of MgTiO$_3$(1.5 nm)/[MgTiO$_3$(6.6 nm), Mg-Ir-O(1.0 nm)]$_3$ /Al$_2$O$_3$. This structural model is consistent with the STEM result shown in Fig. 3(a). In addition, no peaks of impurity phases such as MgO or IrO$_2$ were observed in x-ray diffraction, as shown in the Supplemental Material [56]. These results support formation of a layered structure of IrO$_6$ honeycomb in the superlattice.

We conducted XPS measurements to detect the electronic states of the ilmenite-type oxide heterostructure of Mg-Ir-O/MgTiO$_3$. Since XPS dominantly characterizes the surface region, the sample of Mg-Ir-O(1 nm)/MgTiO$_3$(20 nm)/Al$_2$O$_3$(0001), whose schematics are shown in Fig. 4(a), was applied to the measurements instead of the superlattice discussed in Fig. 3. The lattice formation of Mg-Ir-O (1 nm) on MgTiO$_3$ is expectedly consistent to that in superlattice owing to the epitaxial stabilization coming from oxygen lattices of ilmenite structure. Figure 4(b) shows the XPS result on the Ir 4f core levels. References of IrX$_3$ (X = Cl, Br, and I) for Ir^{3+}, IrO$_2$ for Ir^{4+}, and Ir metal taken from the averages of the peak positions in the NIST X-ray Photoelectron Spectroscopy Database [60] are also plotted. We conducted curve fitting of the spectrum by a function composed of two Voigt functions for peaks and a Shirley function for background. As shown in Fig. 4(b), the fitted function agreed well with the measured data. This result indicates that the Mg-Ir-O film had one chemical state of Ir and that there was nearly no peak from other chemical states. Therefore, in terms of chemical states of Ir, the Mg-Ir-O film was uniform and didn't have a surface state. Comparing the peak energy 61.71 eV of 4$f_{7/2}$ with those of IrO$_2$ in the XPS database [60], we concluded that the

chemical state of Ir was probably tetravalent. To conclude it more surely, we need further measurements, for example, of near-edge x-ray absorption fine structure. The peak shapes were symmetric, unlike the asymmetric peaks of Ir and IrO$_2$ reported in the previous study [61]. These symmetric peak shapes of the Mg-Ir-O film suggest few conduction carriers [61]. To examine additionally the Ti^{4+} in the bottom layer of MgTiO$_3$, the XPS result on the Ti 2p core levels are also compared in Fig. 4(c), with references of Ti 2$p_{3/2}$ of TiO$_2$, Ti$_2$O$_3$, TiO, and Ti metal based on the same database [60]. The spectrum shows a clear pair of the Ti 2$p_{3/2}$ and 2$p_{1/2}$ peaks, indicating that there was little valence fluctuation of Ti ions in the sample [62]. Although the Ti 2$p_{3/2}$ peak of the heterostructure is close to the peak energies of both TiO$_2$ and Ti$_2$O$_3$, the valence of Ti ions should be Ti^{4+} because of crystallization of the ilmenite structure. By applying XPS, the valence of Ir in Mg-Ir-O film stabilized on ilmenite-type MgTiO$_3$ is clearly detected as Ir^{4+}, which leads to the minimum requirement for the Ir $J_{eff} = 1/2$ Mott insulating state.

The DOS at the Fermi level reflects the distinct feature whether insulator or metal. The top panel of Fig. 4(d) shows theoretically calculated DOS of IrO$_6$ honeycomb monolayer near the Fermi level. A gap at the Fermi level is located in the middle of the Ir $j_{eff} = 1/2$ states. Other valence states correspond with the Ir $j_{eff} = 3/2$ and O 2p states. The experimental result of the Mg-Ir-O/MgTiO$_3$ heterostructure is compared in the second top panel. In the result, Ir 5d valence bands are clearly observed below the Fermi level. The energy spectrum of the Ir 5d and O 2p bands shows good agreement with the calculated DOS. Other experimental references on layered honeycomb Na$_2$IrO$_3$ [38] and rutile IrO$_2$ [63] are compared in the bottom two panels. The XPS result of the Mg-Ir-O film is consistent with that of Na$_2$IrO$_3$ and distinct from that of IrO$_2$. The spectrum of IrO$_2$ has finite intensity at the Fermi level, reflecting its metallic electronic states, and has clearly split Ir 5d peaks at the energy levels different from those of Mg-Ir-O and Na$_2$IrO$_3$. These similarities between Mg-Ir-O and Na$_2$IrO$_3$ and differences between Mg-Ir-O and IrO$_2$ also indicate that the electronic states of the Ir in Mg-Ir-O/MgTiO$_3$ heterostructure are mostly consistent to the Na$_2$IrO$_3$ with IrO$_6$ honeycomb structures. The approximately 0.15 normalized intensity at the Fermi level was observed in the Mg-Ir-O/MgTiO$_3$ heterostructure, which is roughly ten times larger than that of 0.013 in Na$_2$IrO$_3$ and less than 30% of ∼0.54 in IrO$_2$. Because the main peak at 1.4 eV of Mg-Ir-O well agrees with that of Na$_2$IrO$_3$ but not IrO$_2$, the difference at the Fermi level may come from the clustered IrO$_6$ or inhomogeneous Ir-O bonds discussed in Fig. 2(d). In fact, the value of electrical resistance of the heterostructure superlattice was >500 MΩ, which is in clear contrast to conducting IrO$_2$ thin films [64]. These results indicate that the electronic states of the Mg-Ir-O/MgTiO$_3$ heterostructure certainly host the formation of the $J_{eff} = 1/2$ Mott insulating electronic state, which is compatible to that of ideal IrO$_6$ honeycomb monolayer. Considering the results on the heterostructure, in the superlattice the electronic structure of Ir may expectedly be closer to the ideal situation of $J_{eff} = 1/2$ insulating state.
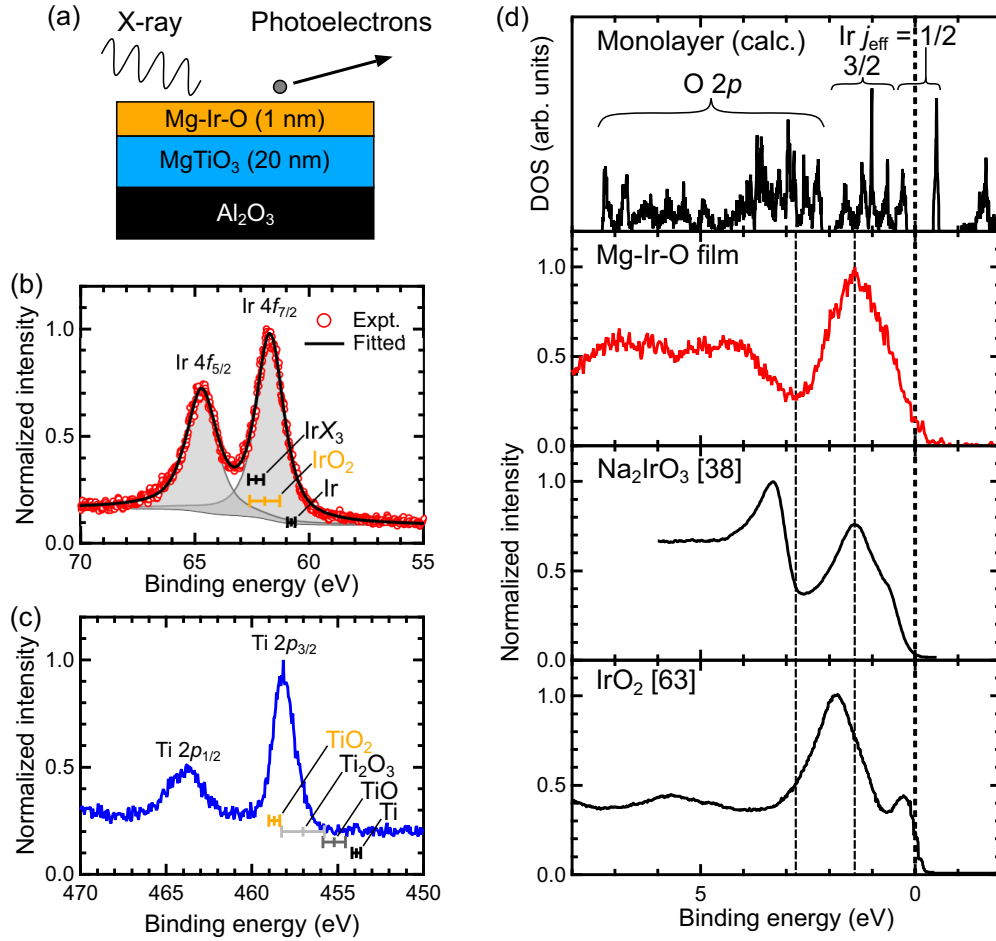
FIG. 4. Electronic states characterized by x-ray photoelectron spectroscopy. (a) A cross-sectional schematic of stacking structure of the sample applied to the XPS measurements. (b) Ir $4f$ core-level spectrum. (c) Ti $2p$ core-level spectrum. (d) Top: Theoretically calculated DOS of IrO_6 honeycomb monolayer. Second top: Valence band spectrum of the Mg-Ir-O film. Second bottom: Photoelectron spectrum of Na_2IrO_3 reproduced from Ref. [38]. Bottom: Photoelectron spectrum of IrO_2 reproduced from Ref. [63].

IV. DISCUSSION

By material design with the theoretical band calculations, the electronic states of ilmenite $MgIrO_3$ and IrO_6 honeycomb monolayer are expected to host the $J_{eff} = 1/2$ Mott insulating state. Although it is difficult to synthesize the metastable phase of ilmenite $MgIrO_3$ in bulk, materialization of single-crystalline $MgIrO_3$ and IrO_6 honeycomb monolayer in superlattice is an attracting research topic. In this study we fabricated Mg-Ir-O/$MgTiO_3$ superlattices to stabilize IrO_6 honeycomb monolayer based on the ilmenite-type structure of $MgTiO_3$. Although the structural inhomogeneity with wavy layered structure was observed in the STEM images, the electronic states of the Mg-Ir-O/$MgTiO_3$ heterostructure clearly demonstrate the Ir $5d$ bands with gap formation in the XPS results, supporting formation of the $J_{eff} = 1/2$ Mott insulating state. Although the inhomogeneous IrO_6 structure may induce both the expected Mott insulating state and the unexpected metallic state like IrO_2, the IrO_6 honeycomb in ilmenite structure is mainly stabilized in superlattice, providing the consistent XPS peak energy at 1.4 eV to that in Na_2IrO_3. Combining the theoretical band calculation, the insulating feature of superlattice likely originates from the $J_{eff} = 1/2$

Mott insulating state. Judging from these results, Ir ions in the superlattices form an IrO_6 honeycomb structure.

We attribute the inhomogeneity in the lateral directions to the thickness imperfection of the Mg-Ir-O layers in the lateral direction. The atomic force microscope (AFM) image of the $MgTiO_3$ single layer film as shown in the Supplemental Material [56] indicates that the bottom $MgTiO_3$ layer was flat. Therefore, the thickness imperfection of the Mg-Ir-O layers resulted in the inhomogeneous IrO_6 layers. However, the thickness imperfection is not critical to our discussion about the formation of a Mott insulating state, because both electronic states of bulk ilmenite $MgIrO_3$ and that of monolayer IrO_6 show a consistent $J_{eff} = 1/2$ Mott insulating state as shown in the Supplemental Material [56]. In contrast, the structural inhomogeneity due to the intersite mixing of Mg and Ir may induce the broadening of Ir bonding state as observed in Fig. 4(d).

To further evaluate the electronic states of Mg-Ir-O superlattices in terms of split bands of the Ir $5d$ states, optical absorption measurements are effective because thin films are applicable to examine the band-to-band excitations directly without the Kramers-Kronig relations. In addition to the XPS results shown in Fig. 4, a split spectrum of optical

absorption will evidence the $J_{\text{eff}} = 1/2$ Mott insulating state and the Kitaev honeycomb magnetism. According to the previous studies on absorption spectra of bulk crystals of Na$_2$IrO$_3$, which is a representative example of the $J_{\text{eff}} = 1/2$ Mott insulators composed of IrO$_6$ honeycomb layers, the broad peaks of absorption relating to the $j_{\text{eff}} = 1/2$ and 2/3 states of Ir 5d electrons were clearly observed below 2.5 eV [38,65]. In the Supplemental Material [56], our attempts of optical spectroscopy of the Mg-Ir-O superlattice are summarized, although the results were not conclusive. To conclude formation of the $J_{\text{eff}} = 1/2$ split bands as the Kitaev honeycomb model, we need to improve uniformity of thickness and increase the repetition cycles in the superlattice for amplifying the optical absorption of Ir 5d states. Considering the present status of our superlattices, we remain these improvements in future study. Bulk-compatible methods of characterization, such as measurements of magnetization and heat capacity, are difficult to apply to thin films due to dominant signals of substrates. Instead, thin-film-compatible methods such as measurements of Raman scattering and fabrication of spin transport devices related to the Majorana fermions may be examined using these heterostructures in the future.

V. CONCLUSIONS

We demonstrate formation of IrO$_6$ honeycomb monolayers by the pulsed-laser deposition technique, leading to the $J_{\text{eff}} = 1/2$ Mott insulating state in Mg-Ir-O/MgTiO$_3$ superlattices. The valence state of Ir^{4+} and insulating band structures were detected by XPS of Mg-Ir-O/MgTiO$_3$ heterostructure. Although detection of Ir 5$d - 5d$ optical transitions remains

a future problem, Mg-Ir-O stabilized in the superlattices is a good candidate of the Kitaev honeycomb magnet. By applying the superlattice technique, Ir or Ru honeycomb structures would be an intriguing platform with the various magnetic ilmenite oxides such antiferromagnetic MnTiO$_3$ and CoTiO$_3$ [33,66,67] to tune the Kitaev interaction via interface interaction and/or lattice strain [35]. Further controllability based on the thin-film techniques will open avenues to address the Kitaev honeycomb magnet and its Majorana physics.

[1] A. Kitaev, Anyons in an exactly solved model and beyond, Ann. Phys. **321**, 2 (2006).

[2] G. Jackeli and G. Khaliullin, Mott insulators in the strong spin-orbit coupling limit: From Heisenberg to a quantum compass and Kitaev models, Phys. Rev. Lett. **102**, 017205 (2009).

[3] H. Takagi, T. Takayama, G. Jackeli, G. Khaliullin, and S. E. Nagler, Concept and realization of Kitaev quantum spin liquids, Nat. Rev. Phys. **1**, 264 (2019).

[4] Y. Motome and J. Nasu, Hunting Majorana fermions in Kitaev magnets, J. Phys. Soc. Jpn. **89**, 012002 (2020).

[5] L. Savary and L. Balents, Quantum spin liquids: A review, Rep. Prog. Phys. **80**, 016502 (2017).

[6] Y. Singh and P. Gegenwart, Antiferromagnetic Mott insulating state in single crystals of the honeycomb lattice material Na$_2$IrO$_3$, Phys. Rev. B **82**, 064412 (2010).

[7] K. Kitagawa, T. Takayama, Y. Matsumoto, A. Kato, R. Takano, Y. Kishimoto, S. Bette, R. Dinnebier, G. Jackeli, and H. Takagi, A spin-orbital-entangled quantum liquid on a honeycomb lattice, Nature (London) **554**, 341 (2018).

[8] P. Lampen-Kelley, S. Rachel, J. Reuther, J.-Q. Yan, A. Banerjee, C. A. Bridges, H. B. Cao, S. E. Nagler, and D. Mandrus, Anisotropic susceptibilities in the honeycomb Kitaev system α-RuCl$_3$, Phys. Rev. B **98**, 100403(R) (2018).

[9] F. Freund, S. C. Williams, R. D. Johnson, R. Coldea, P. Gegenwart, and A. Jesche, Single crystal growth from separated educts and its application to lithium transition-metal oxides, Sci. Rep. **6**, 35362 (2016).

[10] H. B. Cao, A. Banerjee, J.-Q. Yan, C. A. Bridges, M. D. Lumsden, D. G. Mandrus, D. A. Tennant, B. C. Chakoumakos, and S. E. Nagler, Low-temperature crystal and magnetic structure of α-RuCl$_3$, Phys. Rev. B **93**, 134423 (2016).

[11] A. Banerjee, J. Yan, J. Knolle, C. A. Bridges, M. D. Stone, D. G. Mandrus, D. A. Tennant, R. Moessner, and S. E. Nagler, Neutron scattering in the proximate quantum spin liquid α-RuCl$_3$, Science **356**, 1055 (2017).

[12] L. J. Sandilands, Y. Tian, K. W. Plumb, Y.-J. Kim, and K. S. Burch, Continuum and possible fractionalized excitations in α-RuCl$_3$, Phys. Rev. Lett. **114**, 147201 (2015).

[13] J. Nasu, J. Knolle, D. L. Kovrizhin, Y. Motome, and R. Moessner, Fermionic response from fractionalization in an insulating two-dimensional magnet, Nat. Phys. **12**, 912 (2016).

[14] Y. Kasahara, T. Ohnishi, Y. Mizukami, O. Tanaka, S. Ma, K. Sugii, N. Kurita, H. Tanaka, J. Nasu, Y. Motome, T. Shibauchi, and Y. Matsuda, Majorana quantization and half-integer thermal quantum Hall effect in a Kitaev spin liquid, Nature (London) **559**, 227 (2018).

[15] L. E. Chern, E. Z. Zhang, and Y. B. Kim, Sign structure of thermal Hall conductivity and topological magnons for in-plane field polarized Kitaev magnets, Phys. Rev. Lett. **126**, 147201 (2021).

[16] E. Z. Zhang, L. E. Chern, and Y. B. Kim, Topological magnons for thermal Hall transport in frustrated magnets with bond-dependent interactions, Phys. Rev. B **103**, 174402 (2021).

[17] T. Minakawa, Y. Murakami, A. Koga, and J. Nasu, Majorana-mediated spin transport in Kitaev quantum spin liquids, Phys. Rev. Lett. **125**, 047204 (2020).

[18] J. Nasu, Y. Murakami, and A. Koga, Scattering phenomena for spin transport in a Kitaev spin liquid, Phys. Rev. B **106**, 024411 (2022).

[19] T. Misawa, J. Nasu, and Y. Motome, Interedge spin resonance in the Kitaev quantum spin liquid, Phys. Rev. B **108**, 115117 (2023).

[20] Y. Kato, J. Nasu, M. Sato, T. Okubo, T. Misawa, and Y. Motome, Spin Seebeck effect as a probe for Majorana fermions in Kitaev spin liquids, Phys. Rev. X **15**, 011050 (2025).

[21] M. Carrega, I. J. Vera-Marun, and A. Principi, Tunneling spectroscopy as a probe of fractionalization in two-dimensional magnetic heterostructures, Phys. Rev. B **102**, 085412 (2020).

[22] J. Feldmeier, W. Natori, M. Knap, and J. Knolle, Local probes for charge-neutral edge states in two-dimensional quantum magnets, Phys. Rev. B **102**, 134423 (2020).

[23] R. G. Pereira and R. Egger, Electrical access to Ising anyons in Kitaev spin liquids, Phys. Rev. Lett. **125**, 227202 (2020).

[24] E. J. König, M. T. Randeria, and B. Jäck, Tunneling spectroscopy of quantum spin liquids, Phys. Rev. Lett. **125**, 267206 (2020).

[25] M. Udagawa, S. Takayoshi, and T. Oka, Scanning tunneling microscopy as a single Majorana detector of Kitaev's chiral spin liquid, Phys. Rev. Lett. **126**, 127201 (2021).

[26] D. Weber, L. M. Schoop, V. Doppel, J. M. Lippmann, J. Nuss, and B. V. Lotsch, Magnetic properties of restacked 2D spin 1/2 honeycomb $RuCl_3$ nanosheets, Nano Lett. **16**, 3578 (2016).

[27] M. Grönke, P. Schmidt, M. Valldor, S. Oswald, D. Wolf, A. Lubk, B. Büchner, and S. Hampel, Chemical vapor growth and delamination of α-$RuCl_3$ nanosheets down to the monolayer limit, Nanoscale **10**, 19014 (2018).

[28] B. Zhou, Y. Wang, G. B. Osterhoudt, P. Lampen-Kelley, D. Mandrus, R. He, K. S. Burch, and E. A. Henriksen, Possible structural transformation and enhanced magnetic fluctuations in exfoliated $\alpha-RuCl_3$, J. Phys. Chem. Solids **128**, 291 (2019).

[29] S. Mashhadi, Y. Kim, J. Kim, D. Weber, T. Taniguchi, K. Watanabe, N. Park, B. Lotsch, J. H. Smet, M. Burghard, and K. Kern, Spin-split band hybridization in graphene proximitized with α-$RuCl_3$ nanosheets, Nano Lett. **19**, 4659 (2019).

[30] B. Zhou, J. Balgley, P. Lampen-Kelley, J.-Q. Yan, D. G. Mandrus, and E. A. Henriksen, Evidence for charge transfer and proximate magnetism in graphene-α-$RuCl_3$ heterostructures, Phys. Rev. B **100**, 165426 (2019).

[31] D. J. Rizzo, B. S. Jessen, Z. Sun, F. L. Ruta, J. Zhang, J.-Q. Yan, L. Xian, A. S. McLeod, M. E. Berkowitz, K. Watanabe, T. Taniguchi, S. E. Nagler, D. G. Mandrus, A. Rubio, M. M. Fogler, A. J. Millis, J. C. Hone, C. R. Dean, and D. N. Basov, Charge-transfer plasmon polaritons at graphene/α-$RuCl_3$ interfaces, Nano Lett. **20**, 8438 (2020).

[32] D. Hirai, J. Matsuno, and H. Takagi, Fabrication of (111)-oriented $Ca_{0.5}Sr_{0.5}IrO_3$/$SrTiO_3$ superlattices—A designed playground for honeycomb physics, APL Mater. **3**, 041508 (2015).

[33] K. Miura, K. Fujiwara, K. Nakayama, R. Ishikawa, N. Shibata, and A. Tsukazaki, Stabilization of a honeycomb lattice of

IrO_6 octahedra by formation of ilmenite-type superlattices in $MnTiO_3$, Commun. Mater. **1**, 55 (2020).

[34] K. Nakazawa, Y. Kato, and Y. Motome, Asymmetric modulation of Majorana excitation spectra and nonreciprocal thermal transport in the Kitaev spin liquid under a staggered magnetic field, Phys. Rev. B **105**, 165152 (2022).

[35] Y.-F. Zhao, S.-H. Jang, and Y. Motome, Spin-orbit coupled insulators and metals on the verge of Kitaev spin liquids in ilmenite heterostructures, arXiv:2403.09112v1.

[36] B. J. Kim, H. Jin, S. J. Moon, J.-Y. Kim, B.-G. Park, C. S. Leem, J. Yu, T. W. Noh, C. Kim, S.-J. Oh, J.-H. Park, V. Durairaj, G. Cao, and E. Rotenberg, Novel $J_{eff} = 1/2$ Mott state induced by relativistic spin-orbit coupling in Sr_2IrO_4, Phys. Rev. Lett. **101**, 076402 (2008).

[37] W. Witczak-Krempa, G. Chen, Y. B. Kim, and L. Balents, Correlated quantum phenomena in the strong spin-orbit regime, Ann. Rev. Cond. Matter Phys. **5**, 57 (2013).

[38] R. Comin, G. Levy, B. Ludbrook, Z.-H. Zhu, C. N. Veenstra, J. A. Rosen, Y. Singh, P. Gegenwart, D. Stricker, J. N. Hancock, D. van der Marel, I. S. Elfimov, and A. Damascelli, Na_2IrO_3 as a novel relativistic Mott insulator with a 340-meV gap, Phys. Rev. Lett. **109**, 266406 (2012).

[39] Y. Haraguchi, C. Michioka, A. Matsuo, K. Kindo, H. Ueda, and K. Yoshimura, Magnetic ordering with an XY-like anisotropy in the honeycomb lattice iridates $ZnIrO_3$ and $MgIrO_3$ synthesized via a metathesis reaction, Phys. Rev. Mater. **2**, 054411 (2018).

[40] M. Negishi, K. Fujiwara, and A. Tsukazaki, Composition tuning of Mg/Ir ratio and crystallization of a spinel-related structure in Mg-Ir-O films by pulsed-laser deposition, Thin. Solid. Films **769**, 139740 (2023).

[41] M. Negishi, K. Fujiwara, and A. Tsukazaki, Formation of ilmenite-type single-crystalline $MgTiO_3$ thin films by pulsed-laser deposition, AIP Adv. **11**, 125125 (2021).

[42] P. Giannozzi, O. Andreussi, T. Brumme, O. Bunau, M. B. Nardelli, M. Calandra, R. Car, C. Cavazzoni, D. Ceresoli, M. Cococcioni, N. Colonna, I. Carnimeo, A. D. Corso, D. de Gironcoli, P. Delugas, R. A. DiStasio, Jr., A. Ferretti, A. Floris, G. Fratesi, G. Fugallo *et al.*, Advanced capabilities for materials modelling with QUANTUM ESPRESSO, J. Phys.: Condens. Matter **29**, 465901 (2017).

[43] A. I. Liechtenstein, V. I. Anisimov, and J. Zaanen, Density-functional theory and strong interactions: Orbital ordering in Mott-Hubbard insulators, Phys. Rev. B **52**, R5467 (1995).

[44] N. Marzari and D. Vanderbilt, Maximally localized Wannier functions for composite energy bands, Phys. Rev. B **56**, 12847 (1997).

[45] I. Souza, N. Marzari, and D. Vanderbilt, Maximally localized Wannier functions for entangled energy bands, Phys. Rev. B **65**, 035109 (2001).

[46] A. A. Mostofi, J. R. Yates, G. Pizzi, Y.-S. Lee, I. Souza, D. Vanderbilt, and N. Marzari, An updated version of Wannier90: A tool for obtaining maximally-localized Wannier functions, Comput. Phys. Commun. **185**, 2309 (2014).

[47] S.-H. Jang and Y. Motome, Electronic and magnetic properties of iridium ilmenites $AIrO_3$ (A = Mg, Zn, and Mn), Phys. Rev. Mater. **5**, 104409 (2021).

[48] G. Kresse and J. Hafner, *Ab initio* molecular dynamics for liquid metals, Phys. Rev. B **47**, 558(R) (1993).

[49] G. Kresse and J. Hafner, *Ab initio* molecular-dynamics simulation of the liquid-metal–amorphous-semiconductor transition in germanium, Phys. Rev. B **49**, 14251 (1994).

[50] G. Kresse and J. Furthmüller, Efficiency of *ab-initio* total energy calculations for metals and semiconductors using a plane-wave basis set, Comput. Mater. Sci. **6**, 15 (1996).

[51] G. Kresse and J. Furthmüller, Efficient iterative schemes for *ab initio* total-energy calculations using a plane-wave basis set, Phys. Rev. B **54**, 11169 (1996).

[52] G. Kresse and D. Joubert, From ultrasoft pseudopotentials to the projector augmented-wave method, Phys. Rev. B **59**, 1758 (1999).

[53] S. P. Ong, L. Wang, B. Kang, and G. Ceder, The Li − Fe − P−O$_2$ phase diagram from first principles calculations, Chem. Mater. **20**, 1798 (2008).

[54] S. P. Ong, A. Jain, G. Hautier, B. Kang, and G. Ceder, Thermal stabilities of delithiated olivine MPO$_4$ (M = Fe, Mn) cathodes investigated using first principles calculations, Electrochem. Commun. **12**, 427 (2002).

[55] R. Ishikawa, A. R. Lupini, S. D. Findlay, and S. J. Pennycook, Quantitative annular dark field electron microscopy using single electron signals, Microsc. Microanal. **20**, 99 (2014).

[56] See Supplemental Material at http://link.aps.org/supplemental/10.1103/gz4v-8mds for the list of samples and experiments performed for them; the calculated total and projected DOS-s of ilmenite MgIrO3 and monolayer; the ADF and ABF images around Mg-Ir-O layer; the x-ray diffraction patterns of the Mg-Ir-O/MgTiO$_3$ superlattice and the Mg-Ir-O/MgTiO$_3$ heterostructure; the AFM image of a MgTiO$_3$ film on α-Al$_2$O$_3$(001) substrate; the XPS survey scan of the Mg-Ir-O/MgTiO$_3$ heterostructure; the XPS of the Mg-Ir-O/MgTiO$_3$ heterostructure measured with pass energy of 200 and 100 eV; the calclated DOS of MgIrO$_3$ monolayer and ilmenite bulk and valence band XPS of the Mg-Ir-O film on MgTiO$_3$ buffer; and a summary of the results on optical spectroscopy.

[57] A. Jain, S. P. Ong, G. Hautier, W. Chen, W. D. Richards, S. Dacek, S. Cholia, D. Gunter, D. Skinner, G. Ceder, and A. K. Persson, The Materials Project: A materials genome approach to accelerating materials innovation, APL Mater. **1**, 011002 (2013).

[58] A. Jain, G. Hautier, S. P. Ong, C. Moore, C. Fischer, K. Persson, and G. Ceder, Formation enthalpies by mixing GGA and GGA + U calculations, Phys. Rev. B **84**, 045115 (2011).

[59] S. J. Pennycook and L. A. Boatner, Chemically sensitive structure-imaging with a scanning transmission electron microscope, Nature (London) **336**, 565 (1988).

[60] NIST X-ray Photoelectron Spectroscopy Database, NIST Standard Reference Database Number 20, National Institute of Standards and Technology, Gaithersburg, MD (2000), DOI: https://dx.doi.org/10.18434/T4T88K (retrieved May 30, 2023).

[61] V. Pfeifer, T. E. Jones, J. J. Velasco Vélez, C. Massué, R. Arrigo, D. Teschner, F. Girgsdies, M. Scherzer, M. T. Greiner, J. Allan, M. Hashagen, G. Weinberg, S. Piccinin, M. Hävecker, A. Knop-Gericke, and R. Schlögl, The electronic structure of iridium and its oxides, Surf. Interface Anal. **48**, 261 (2016).

[62] K. Morikawa, T. Mizokawa, A. Fujimori, Y. Taguchi, and Y. Tokura, Photoemission spectral weight distribution in Y$_{1-x}$Ca$_x$TiO$_3$, Phys. Rev. B **54**, 8446 (1996).

[63] J. M. Kahk, C. G. Poll, F. E. Oropeza, J. M. Ablett, D. Céolin, J.-P. Rueff, S. Agrestini, Y. Utsumi, K. D. Tsuei, Y. F. Liao, F. Borgatti, G. Panaccione, A. Regoutz, R. G. Egdell, B. J. Morgan, D. O. Scanlon, and D. J. Payne, Understanding the electronic structure of IrO$_2$ using hard-x-ray photoelectron spectroscopy and density-functional theory, Phys. Rev. Lett. **112**, 117601 (2014).

[64] S. Nair, Z. Yang, K. Storr, and B. Jalan, High-mobility carriers in epitaxial IrO$_2$ films grown using hybrid molecular beam epitaxy, Nano Lett. **24**, 10850 (2024).

[65] C. H. Sohn, H.-S. Kim, T. F. Qi, D. W. Jeong, H. J. Park, H. K. Yoo, H. H. Kim, J.-Y. Kim, T. D. Kang, D.-Y. Cho, G. Cao, J. Yu, S. J. Moon, and T. W. Noh, Mixing between $J_{\mathrm{eff}} = 1/2$ and 3/2 orbitals in Na$_2$IrO$_3$: A spectroscopic and density functional calculation study, Phys. Rev. B **88**, 085125 (2013).

[66] K. Miura, K. Fujiwara, J. Shiogai, T. Nojima, and A. Tsukazaki, Electrical detection of the antiferromagnetic transition in MnTiO$_3$ ultrathin films by spin Hall magnetoresistance, J. Appl. Phys. **127**, 103903 (2020).

[67] K. Yoshimatsu, H. Mashiko, N. Umezawa, K. Horiba, and A. Ohtomo, Electronic structures and photoanodic properties of ilmenite-type MTiO$_3$ epitaxial films (M = Mn, Fe, Co, Ni), J. Phys. Chem. C **121**, 18717 (2017).